A new regression model to predict BIPV cell temperature for various climates using a high-resolution CFD microclimate model

Ruijun Zhang[a], Yangyu Gan[a], Parham A. Mirzaei[a]*

[a] Architecture and Built Environment Department, The University of Nottingham, Nottingham, NG7 2RD, UK

* Corresponding author: parham.mirzaei_ahranjani@nottingham.ac.uk

Abstract

Understanding of cell temperature of Building Integrated Photovoltaics (BIPV) is essential in the calculation of their conversion efficiency, durability and installation costs. Current PV cell temperature models mainly fail to provide accurate predictions in complex arrangement of BIPVs under various climatic conditions. To address this limitation, this paper proposes a new regression model for prediction of the BIPV cell temperature in various climates and design conditions, including the effects of relative PV position to the roof edge, solar radiation intensity, wind speed, and wind direction. To represent the large number of possible climatic and design scenarios, the advanced technique of Latin Hypercube Sampling was firstly utilized to reduce the number of investigated scenarios from 13,338 to 374. Then, a high-resolution validated full-scale 3-dimensional Computational Fluid Dynamics (CFD) microclimate model was developed for modelling of BIPV's cell temperature, and then was applied to model all the reduced scenarios. A nonlinear multivariable regression model was afterward fit to this population of 374 sets of CFD simulations. Eventually, the developed regression model was evaluated with new sets of unused climatic and design data when a high agreement with a mean discrepancy of 3% between the predicted and simulated BIPV cell temperatures was observed.

Keywords: Building, BIPV, Latin Hypercube Sampling, Regression, CFD

Nomenclature

Symbol	Description	Units	Symbol	Description	Units
T_c	PV cell temperature	K	T_a	Ambient air temperature	K
k_r	Ross coefficient	$m^2 K/W$	G_t	Solar irradiance	W/m^2
U	Wind speed	m/s	C_a, C_b	SNL model coefficients	
ΔT	Difference of T_c and back surface temperature under G_o	K	x, y, z	Computational cell length in three dimensions	m
L, W, H	Dimension of objects	m	u	Fluid velocity	m/s
p	Fluid pressure	pa	Q'_c	Convective heat flux	W/m^2
G_o	Reference solar radiation	W/m^2	ρ	Air density	kg/m^3
$\vec{g}$	Gravitational acceleration	m/s^2	$\bar{\bar{\tau}}_{eff}$	Effective stress tensor	
μ_{eff}	Effective viscosity	m^2/s	$\bar{I}$	Unit tensor	
μ_t	Eddy viscosity	m^2/s	μ	Sum of molecular viscosity	m^2/s
ρ_0	Constant density under operating temperature T_0	kg/m^3	G_k	Mean velocity gradient contributed to k	W/m^3
β	Thermal expansion	1/K	k	Turbulence kinetic energy	J/kg
ε	Turbulence dissipation rate	m^2/s^3	T_0	Operating temperature	K

Symbol	Description	Unit	Symbol	Description	Unit
G_b	Buoyancy contributed to k	W/m^3	S_k	User-defined source of k	
$\sigma_k, \sigma_\varepsilon$	Prandtl number for k and ε		C_μ	Model constant	
$C_{1\varepsilon}, C_{2\varepsilon}$	Model constants		S_ε	User-defined source of ε	
E	Energy of unit mass component	m^2/s^2	$\bar{h}$	Sensitivity enthalpy	m^2/s^2
λ_f	Flow thermal conductivity	W/mK	λ_t	Turbulence conductivity	W/mK
$\bar{h}_j \vec{J}_j$	Enthalpy transportation of diffusion	W/m^2	λ	Coefficient of thermal conductivity	W/mK
S_h	User-defined source of energy		S_r	Solar load	W/m^3
Q'	Heat flux	W/m^2	$\varepsilon_{m,r}$	Emissivity of exposed roof surface	
σ	Stefan-Boltzmann constant		T_{sky}	Sky temperature	K
T_r	Roof temperature	K	$\varepsilon_{m,s}$	Sky emissivity	
U_z	Local flow speed at H_z	m/s	U_{met}	Meteorological wind velocity	m/s
H_Z	Local height	m	H_{met}	Height of meteorological station	m
α	Wind shear exponent		I_z	Local turbulence intensity	
δ_G	Terrain boundary thickness	m	k_z	Local turbulence kinetic energy	m^2/s^2
ε_z	Local turbulence dissipation rate	m^3/s^3	L_a	Vertical temperature gradient	K/m
E_r	Radius of the Earth	m	PI	PV position index	
θ	Relative wind angle	°	N	Population size	
n	Sample size		p_s	Sample proportion	
z_c	Critical value at a given confidence level		l	Distance between bottom edge of PV panel and roof	m
d	Margin of error		R^2	Coefficient of determination	
Y_i	Observed (simulated) value of each sample		$\hat{Y}_i$	Predicted value of each sample	
$\bar{Y}_i$	Mean of all observed value		k_{coeff}	Total number of coefficients in regression	
$RMSE$	Root mean square error		E_1	Relative gap	
$FAC2$	Fraction of predictions within a factor of two of observations				

1. Introduction

The share of renewable energy has increased in the world primary consumptions from 14% of global demands in 1998 to 19.3 % in 2015 (Goldemberg, 2000; Renewable Energy Policy Network for the 21st Century [REN21], 2017). It is expected that renewable energy share takes one quarter of the whole energy market by 2040 with an average annual increase rate of 2.8% (Energy Information Administration [EIA], 2017) with a potential to be expanded over a long-term period of time (up to 30-80% by 2100 according to Panwar, Kaushik, and Kothari (2011)). Among the markets of clean energy, photovoltaic (PV) technologies have shown a promising success during past years while it was predicted to keep permeating with further improvements in PV's performances (REN21, 2017). Solar PVs are vastly integrated or partially integrated to building roofs and façades, known as building integrated photovoltaics (BIPV), converting solar energy into electricity on the site and supporting the building energy demands (Elkarmi & Abu-Shikhah, 2012; Bramanti, 2015).

In ideal experimental conditions, the electrical efficiency of a typical PV system is 15-20 % (Kalogirou, 2014). Accumulative heat impacted on a PV panel leads to the elevation of surface/cell temperature (T_s/T_c) and thereby causes a drop of cell efficiency, normally occurring when operating temperature exceeds 25 °C (Solanki, 2013), with a rate of -0.2 %/°C to -0.45 %/°C for amorphous and crystalline-silicon-based PVs (Kalogirou, 2014). In addition, the high temperature degrades the PV materials and hence shorten their durability, which is expected as 30-35 years for such integrated systems (Bahaj, 2003). This implies that the PV cell temperature should be controlled either with advanced mechanical cooling approaches

or alternatively with natural ventilation, particularly in hot climate where there is a high risk of hot spot formations.

Elkarmi and Abu-Shikhah (2012) recommended an elaborative scrutiny of the installation site before the PV implementation to access an optimum performance. This implies that, to evaluate the reliability and feasibility of a BIPV project, tools are required to assess the near-field airflow around cell surfaces and further to estimate their operating thermal behaviour. Skoplaki and Palyvos (2009) undertook a literature review of methods to determine the PV operating temperate, including implicit and explicit methods. The PV temperature given by the former method depends on some variables relying on temperature, for example, the panel efficiency, while the explicit method calculates temperature directly. In general, it is crucial that these models should include the impact of surrounding environment in their calculations although there were only few developed models finding T_c from its relation with the surrounding environment. Example of such models is an explicit calculation by (Ross Jr, 1976):

$$T_c = T_a + k_r G_t \tag{1}$$

where T_a is the ambient air temperature (K), G_t is solar irradiance $(\mathrm{W/m^2})$ and k_r is Ross coefficient $(\mathrm{m^2 K/W})$; the adapted values of which are summarized from reference data (Nordmann & Clavadetscher, 2003). Another example is a model to predict PV temperature from a nominal operating cell temperature (NOCT) measured in the nominal terrestrial environment (NTE) condition, also known as the standard reference environment, which is specified as 800 W/m² irradiance normal to a free-running device mounted rack with an optimum tilt ventilation against 1m/s wind at an ambient temperature of 20 °C (Markvart & Bogus, 2000):

$$T_c = T_a + \left(T_{c,NOCT} - 20\right)\frac{G_t}{800} \tag{2}$$

where NOCT means the referring variable to the value at the nominal terrestrial environment. Furthermore, a model was developed by Sandia National Laboratories (SNL) (King, Boyson, & Kratochvill, 2004; Skoplaki & Palyvos, 2009), which includes wind speed in its equation:

$$T_c = T_a + G_t \cdot \left(e^{C_a + C_b U}\right) + \frac{G_t}{G_o} \cdot \Delta T \tag{3}$$

where C_a and C_b are the model coefficients determined by the module type and mounting method. U represents the wind speed $(\mathrm{m/s})$, and ΔT is the temperature difference (K) between the solar cell and rear surface measured under a reference solar radiation flux of $G_o = 1000 \ \mathrm{W/m^2}$.

All these models included the effect of solar radiation and ambient temperature. However, the effect of wind speed was only considered by SNL model via empirical coefficients, depending on the module assembles and mountings. The NOCT model only took a default natural ventilation value against the wind of 1m/s whilst the ventilation effect was simply inducted by assigning different array installations in the first model. In conclusion, none of these methods took the influence of stochastic wind directions into the account, which can

be source of a huge discrepancy in the prediction of PV cell temperature. For example, an assessment undertaken by D'Orazio, Perna & Di Giuseppe (2014) within typical Italian climate showed that the deviation between the calculated temperature by NOCT and measurement was up to 12 °C while this value was 8°C between the SNL method and measurement. In another study by Assoa, Gaillard, Ménézo, Negri, & Sauzedde (2018), it was reported that NOCT model significantly overestimated the PV cell temperature while Ross coefficient failed to evaluate the heat dissipation due to the lack in consideration of the site wind conditions.

As another limitation, the current site surveying for BIPV installation was mainly focused on the solar data and overshadowing of surroundings, but seldom considering the wind effect (Bagatelos & Henson, 2012). There were few studies through field measurements that considered variation of weather conditions though entirely focused on wind speed rather than wind direction (Kaldellis, Kapsali, & Kavadias 2014; Gökmen, 2016). Despite of the well understood fact that PVs' natural cooling is impacted by the integration type, building geometry, and district planning with stochastic climates, there is scarce investigation, paying attention to the impact of these factors although difficult to predict, especially in complex urban morphologies. In conclusion, site survey and experimental techniques in measurement of PV cell temperature face a high operating cost and many difficulties for repetitive tests to minimize site-dependent influences, placing them as less preferred options. On the other side, Computational Fluid Dynamics (CFD) technique is considered as a promising approach to deliver quantitative studies due to its high flexibility and accuracy with less operating cost.

*Table 1 Summary of previous CFD studies for the design of BIPVs*

Authors	Type	Dimension	Turbulence model	Investigation
Hemmer, Saad, Popa & Polidori (2017)	BIPV	2D	laminar	Impact of mounting geometry impacts on convection
Wilson and Paul (2011)	BIPV	2D	laminar	
Gan (2009a, 2009b)	BIPV	2D	RNG k-ε turbulence	
Liao et al. (2005)	BIPV/T	2D	k-ε model	Convection beneath/ over PV Impact of:
Jubayer, Karava, & Savory (2010)	BIPV/T	3D	Realizable k-ε / SST k-ω	-Velocity (Liao, et al., 2005; Karava et al., 2012; Zogou & Stapountzis 2012; Zhang, 2017) -Solar radiation (Liao, 2005; Zhang, et al., 2017) -Wind direction (Karava, et al., 2012) -PV tilt (Karava, et al., 2012) -Active cooling at backside (Teo, et al., 2012)
Karava, Jubayer, Savory & Li (2012)	BIPV/T	3D		
Teo, Lee & Hawlader (2012)	PV/T	3D	-	
Zogou and Stapountzis (2012)	BIPV/T	3D	k-ε model	
Zhang, Mirzaei and Carmeliet (2017)	BIPV	3D	Standard k-ε model	
Koyunbaba, Yilmaz & Ulgen (2013)	BIPV	2D	Standard k-ε model	Impact of velocity on thermal behavior
ElSayed (2016)	BIPV	2D	k-ε model	
Mirzaei and Zhang (2015)	BIPV	3D	Standard k-ε model	
Jubayer (2014)	PV	3D	k-ω turbulence	Impact of wind on ground mounted stand-alone PV

CFD has been widely applied to reproduce thermal and velocity patterns around tested panels to find optimal BIPV designs. For example, the critical cavity size was found to be 0.02m by Wilson and Paul (2011), and 0.12-0.15 m and 0.14-0.16 m by Gan (2009a) for multi- and single module systems, respectively. *Table 1* summarizes some of the recent CFD studies related to the design of BIPVs. As it can be seen in *Table 1*, most studies were focused on the cavity, but barely considering the airflow above the cell (Liao, et al., 2005; Gan 2009a, 2009b; Wilson & Paul, 2011; Koyunbaba, et al., 2013); although some investigated the nearfields around, only velocity field was analysed, but no thermal performance was included (Jubayer, et al., 2010; Karava, et al., 2012); furthermore, many of them also simulated the BIPV design in the limited range of variations; for example, only 0-20 degree wind directions were considered in (Karava, et al., 2012). Despite of the mentioned advantageous of CFD techniques in understanding of airflow and temperature fields around BIPVs, it is computationally impractical to investigate BIPVs with a 3D CFD model under a wide range of variation considering all influential parameters under more realistic climatic conditions, therefore, sensitivity tests of integrated PVs to different parameters are required.

Therefore, the aim of this study is to develop a high-resolution regression model to predict BIPVs' cell temperature, including effects of various PV design and climatic scenarios by taking advantage of a full-scale 3D CFD model, validated with a wind tunnel measurement study. The simulations of all these climatic and design scenarios are impractical as the enormous population size required to cover all of them; thus, the goal is to minimize the intensive computational load of the CFD model by only simulation of the representative samples of scenarios determined by using Latin Hypercube Sampling method. To calculate the minimum population size of the sampling method, a sensitivity analysis was initially conducted to reduce the strip amount of each variable. Finally, a new regression model was fit to the simulated scenarios and was successfully evaluated in prediction of the BIPV cell temperature under various climatic and design scenarios. It should be noted that developed CFD in this study is validated with the experimental data and has a high level of reliability and accuracy and will be used to evaluate the performance of the new regression models due to the limitation in access to the realistic experimental data.

2. Methodology
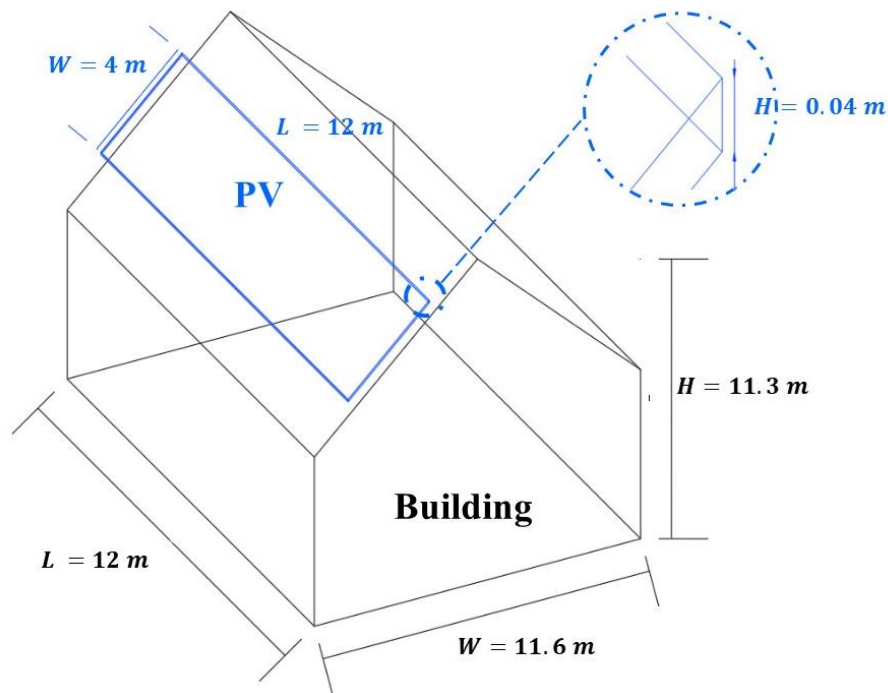
Figure 1 Full-scale BIPV construction

2.1. CFD modelling

2.1.1   Microclimatic and BIPV models

The computational model used in this study was developed from a properly validated CFD model representing BIPV in a wind tunnel experiment (Mirzaei, Paterna & Carmeliet, 2014; Mirzaei & Carmeliet, 2015; Zhang, et al., 2017). The original model was enlarged to a full-scale BIPVs as shown in Figure 1. After removing the radiation simulator, the wind tunnel surfaces were then replaced with a cylindrical microclimate, which have a minor deviation in accuracy from the wind-tunnel model with the rectangular shape (Mirzaei & Carmeliet, 2013), although with a higher flexibility in capturing the stochastic approaching wind. The lateral wall of the cylindrical domain was placed far from the building by at least $15H$ (H is the height of the building) as shown in *Figure 2* in accordance with the best practice guidelines (Tominaga, et al., 2008) to ensure the airflow from different directions reaching a fully developed condition. Also, the lateral wall was divided into multiple planes evenly to be able to assign the approaching winds from different directions. The sky boundary was settled at $5H$ above the building. The basic mesh configuration was generated based on a previous study of (Zhang, et al., 2017) to achieve a high agreement between CFD simulation and wind tunnel experiment. The average uncertainty of computational results of developed model from the measurements was found as 8.0% in overall with 13.2% in the cavity and 7.2% for the normalized velocity in the upstream region (Zhang, et al., 2017). In terms of the temperature field, the accuracy of developed computational model exceeds 95% and 90% for temperature predictions of the BIPV surface and its surrounding airflows, respectively. As only a slight difference is implemented in the quality of both meshes, the new CFD mesh was considered

6

158 to perform similarly as the validated wind tunnel mesh.
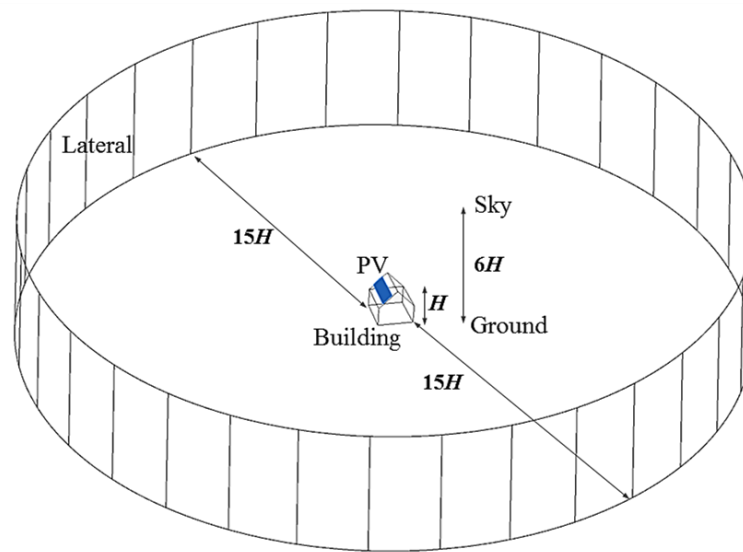
Figure 2 Model of BIPV with cylindrical microclimatic domain

161   A PV panel with the dimensions of 12 m × 4 m × 0.04 m ($L \times W \times H$) was integrated to
162 the pitched roof of a full-size building with dimensions of 12 m × 11.6 m × 11.3 m ($L \times W \times$
163 H). The PV panel covered 50 % of the roof area mounted parallel to the 45 ° inclined roof
164 with an air cavity of 0.3 m; the fixed cavity distance satisfied the suggested minimum value
165 to reduce the occurrence of overheating in the BIPV (Gan, 2009a). There are approximately
166 0.16 million structured cells used to construct the BIPV and its nearby boundary layers (as
167 seen in *Figure 3*) whilst the size of the whole model is about 1.85 million cells in the new
168 mesh.

169 2.1.2 Governing equations

170   ANSYS FLUENT 18.1 was employed for modelling the fluid flow and heat transfer around
171 the PV panels in this study. Standard wall-function treatment was applied to the boundary
172 flow around the wall surfaces where dense inflated boundary layer grids were utilized. For all
173 the simulations, the governing equations were Reynolds Averaged Navier-Stokes (RANS)
174 scheme with the Standard k-ε turbulence model under the steady-state conditions:
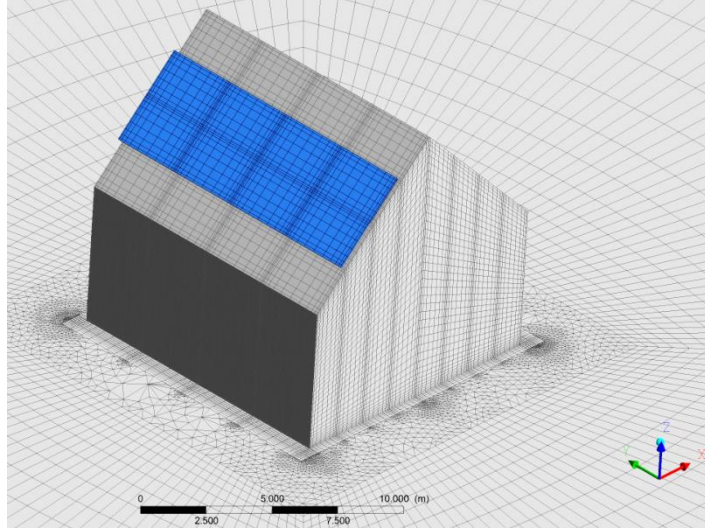
$$\frac{\partial}{\partial x_j}\left(u_j\right) = 0 \tag{4}$$

Figure 3 Computational grids of BIPV

$$\rho u_j \frac{\partial u_i}{\partial x_j} = -\frac{\partial p}{\partial x_i} + \frac{\partial}{\partial x_j} \bar{\bar{\tau}}_{eff} + \rho \vec{g} \tag{5}$$

where u is the airflow velocity (m/s), ρ is the air density (kg/m³), p is the pressure (pa). Subscripts i,j,k represent the three dimensions (i.e. 1, 2 and 3). $\bar{\bar{\tau}}_{eff}$ is the effective stress tensor, which is given by:

$$\bar{\bar{\tau}}_{eff} = \mu_{eff} \left[\left(\frac{\partial u_i}{\partial x_j} + \frac{\partial u_j}{\partial x_i} \right) - \frac{2}{3} \frac{\partial u_i}{\partial x_i} \bar{I} \right] \tag{6}$$

where $\bar{I}$ is the unit tensor and the effective viscosity, μ_{eff} is the sum of the molecular viscosity (μ) and eddy viscosity (μ_t):

$$\mu_{eff} = \mu + \mu_t \tag{7}$$

Term $\rho \vec{g}$ in *Eq. (5)* is representing the gravitational force where the buoyancy effect is reflected. Buossinesq approximation was used to determine the change of air density with temperature in this term:

$$(\rho - \rho_0)g \approx -\rho_0 \beta (T - T_0) \tag{8}$$

where ρ_0 is the constant density under the operating temperature $T_0(\mathrm{K})$ and β is the thermal expansion coefficient (K^{-1}). As $\beta(T - T_0)$ is much less than one in this study, the Boussinesq model is a valid assumption. Moreover, the Standard k-ε model was solved by the following equations for k and ε, respectively:

$$\frac{\partial}{\partial x_i}(\rho k u_i) = \frac{\partial}{\partial x_j} \left[\left(\mu + \frac{\mu_t}{\sigma_k} \right) \frac{\partial k}{\partial x_j} \right] + G_k + G_b - \rho \varepsilon + S_k \tag{9}$$

$$\frac{\partial}{\partial x_i}(\rho \varepsilon u_i) = \frac{\partial}{\partial x_j}\left[\left(\mu + \frac{\mu_t}{\sigma_\varepsilon}\right)\frac{\partial \varepsilon}{\partial x_j}\right] + C_{1\varepsilon}\frac{\varepsilon}{k}G_k - C_{2\varepsilon}\rho\frac{\varepsilon^2}{k} + S_\varepsilon \tag{10}$$

189 where G_k, G_b and S_k are the contributed k by mean velocity gradients, buoyancy and user-
190 defined source, respectively. σ_k and σ_ε are the Prandtl number of turbulence k and ε,
191 respectively. $C_{1\varepsilon}$ and $C_{2\varepsilon}$ are model constants while S_ε represents ε generated by a user-
192 defined source. With this model, the eddy viscosity (μ_t) can be calculated using the
193 turbulence kinetic energy and dissipation rate as follows:

$$\mu_t = C_\mu \rho \frac{k^2}{\varepsilon} \tag{11}$$

194 where the default values of model constants are found as C_μ = 0.09, σ_k = 1.0, σ_ε = 1.3, $C_{1\varepsilon}$ =
195 1.44 and $C_{2\varepsilon}$ = 1.92. The energy of fluid region was also given by the following governing
196 equation:

$$\rho u_j \frac{\partial E}{\partial x_j} = \frac{\partial}{\partial x_j}\left[(\lambda_f + \lambda_t)\frac{\partial T}{\partial x_j}\right] - p\frac{\partial u_j}{\partial x_j} - \frac{\partial}{\partial x_j}\sum_j \bar{h}_j \vec{J}_j + \frac{\partial u_j}{\partial x_j}\bar{\bar{\tau}}_{eff} + S_h \tag{12}$$

197 where $E = \bar{h} - \frac{p}{\rho} + \frac{u^2}{2}$ and $\bar{h}$ is the sensitivity enthalpy (m^2/s^2). λ_f and λ_t are the flow thermal
198 conductivity and turbulence conductivity. Term $\sum_j \bar{h}_j \vec{J}_j$ indicates the enthalpy transportation
199 due to the species diffusion. S_h is the user-defined source of energy.

200 Solar radiation was projected into the PV panel in a normal direction using a solar ray
201 tracing model, which gave the source term in the energy equation of PV solid region as below:

$$\frac{\partial}{\partial x_j}\left(\lambda\frac{\partial T_c}{\partial x_j}\right) + S_r = 0 \tag{13}$$

202 where λ is the thermal conductivity (W/mK), T_c is the PV cell temperature (K) and S_r is the
203 solar load (W/m^3) added to PV cells.

204 The roof of building was insulated from the ambient environment. As the PV panel
205 covered only half of the roof area, the other half was exposed to the sunlight, which may
206 cause overheating over the roof surface. The longwave radiative heat loss to the sky was
207 then introduced at the exposed surfaces by editing the radiation boundary condition heat flux
208 (Q') as:

$$Q' = \varepsilon_{m,r}\sigma(T_{sky}^4 - T_r^4) \tag{14}$$

209 where $\varepsilon_{m,r}$ is the emissivity of the exposed roof surface and σ is Stefan-Boltzmann constant
210 = 5.670367×10^{-8} W/m^{2}K^4. T_{sky} and T_r are the sky and roof temperatures (K), respectively.
211 T_{sky} was set at 285.13 K determined through (Gliah, Kruczek, Gh. Etemad & Thibault, 2011)
212 by $T_{sky} = (\varepsilon_{m,s}T_a^4)^{1/4}$ where T_a is the air temperature set to be 298.15K in this study, and

213 $\varepsilon_{m,s} \approx 0.836$ is the sky emissivity approximated based on a range of the dew point
214 temperature (Chen, Clark, Maloney, Mei & Kasher, 1995).

2.1.3 CFD setup and boundary conditions

216   Solar load was directly applied to the upward PV surface and the exposed roof. An
217 assumption of no participation in solar model was made for the roof area covered by the PV
218 panel and other building surfaces. The velocity pattern at the inflow boundaries was given by
219 the exponent power law (Tominaga, et al., 2008):

$$U_z = U_{met} \left(\frac{H_z}{H_{met}} \right)^{\alpha} \tag{15}$$

220 where U_z is the local wind speed (m/s) at the height of H_z (m). U_{met} is the reference wind
221 velocity (m/s) measured at the meteorological station where the data are collected at the
222 height $H_{met} = 10$ m. $\alpha = 0.2$ is the wind shear exponent, which depends on the terrain
223 description type and it was taken as a suburban terrain in this study. The vertical profiles for
224 k and ε were estimated from the corresponding local turbulence intensity (I_z) given by the
225 following equation (Tominaga, et al., 2008):

$$I_z = 0.1 \left(\frac{H_z}{\delta_G} \right)^{(-\alpha - 0.05)} \tag{16}$$

226 where δ_G is the boundary thickness of a specific terrain taken as 450 m in this study. An
227 acceptable assumption of the local turbulence kinetic energy (k_z) was utilized from I_z for the
228 atmospheric boundary layer flow (Tominaga, et al., 2008):

$$k_z = (I_z U_z)^2 \tag{17}$$

229 The local ε_z values were then determined through:

$$\varepsilon_z = C_\mu^{1/2} k_z \frac{U_{met}}{H_{met}} \alpha \left(\frac{H_z}{H_{met}} \right)^{(\alpha - 1)} \tag{18}$$

230   The air temperature is decreasing along the vertical direction in the troposphere
231 (Department of Energy U.S. [DOE], 2016) and thus its profile was given by:

$$T_{a,z} = T_{a,met} - L_a \left(\frac{E_r H_{met}}{E_r + H_{met}} - \frac{E_r H_z}{E_r + H_z} \right) \tag{19}$$

232 where $T_{a,z}$ (K) is the local air temperature at elevation of H_z (m) from the ground and $T_{a,met}$
233 (K) is the meteorological air temperature at its calculated height of H_{met} (m) in meteorological
234 station of 1.5 m. $L_a = -0.0065$ K/m is the vertical temperature gradient and $E_r = 6356 \times 10^3$ m
235 is the radius of the Earth.

236 *Table 2 CFD boundary conditions*

Boundary	Type	Treatment

Ground / building surfaces	Wall	No-slip and adiabatic Not participate in the solar model Adiabatic/Insulated
Back & lateral surfaces of PV	Wall	No-slip and adiabatic Not participate in the solar model Coupled: zero heat generation
Sky/ laterals of the climatic domain	Symmetry	-
Front surface of PV	Wall	No-slip Absorptivity = 0.9 participate in the solar model Coupled: zero heat generation
Inflow	Velocity inlet	Vertical velocity profile Normal to the boundary Vertical k and ε profiles Vertical temperature profiles participate in the solar model
Outflow	Pressure outlet	Gauge pressure = 0 pa Vertical k and ε profiles Vertical temperature profiles participate in the solar model

237   *Table 2* shows a summary of boundary conditions defined for the computational model in
238   FLUENT 18.1 following recommendations by Mirzaei and Haghighat (2012). The absorptivity
239   of the opaque dark PV surface was taken as 0.9 (Reagan & Acklam, 1979). SIMPLE algorithm
240   was employed to solve the transport equations while all the transport equations were
241   discretized with the second-order upwind scheme except the pressure, which was discretized
242   with the second-order scheme. The convergence criterion was set as 10^{-6} for the energy
243   equation while the values were set as 10^{-4} for the continuity, momentum and turbulence
244   equations.

245   **2.2. Sampling and sensitivity analysis**

246   First, the thermal performance of PV panels was presented using the temperature
247   difference between the cell and ambient (as the reference) temperatures. As a preliminary
248   test, the influence of panel arrangement (stepped or flat) on its thermal performance was
249   found to be insignificant, and thereby, only the flat PV arrangement was chosen to be
250   simulated. Moreover, a new variable, PV position index (PI), was introduced to represent the
251   relative location of the PV panel as the ratio of distance between the bottom and top edges
252   of the PV panel over the roof width as seen in *Figure 4a*:

$$PI = l/L \tag{20}$$

253   where l is the distance between the bottom and top edges of the PV panel. L is the width of
254   the roof. In this study, three relative positions for the PV panel over the roof were considered,
255   including the bottom ($PI = 0$), middle ($PI = 0.25$) and top ($PI = 0.5$) as displayed in *Figure 5*.

256   Then, the investigation was designed to cover ranges of different climatic variables,
257   including solar irradiance, wind direction and wind speed. A standard range of wind speed in
258   Northern hemisphere is between 0-20 $\mathrm{m/s}$ with a highest frequency band lies in the range of

259   0-5m/s (Vautard, Cattiaux, Yiou, Thépaut & Ciais, 2010). However, the lowest wind speed
260   was set as 0.5m/s rather than 0m/s, considering slow CFD convergence and k-ε turbulence
261   weakness in low Reynolds conditions. Furthermore, the solar irradiance was assumed to be
262   uniformly distributed from 80 W/m^2 to 1,200 W/m^2 (King, et al., 2004). The stochastic relative
263   wind angle was treated from $\theta = 0°$ to $\theta = 180°$, where $\theta = 0°$ represents the direction of the
264   BIPV orientation as shown in *Figure 4b.*

(a)   (b)
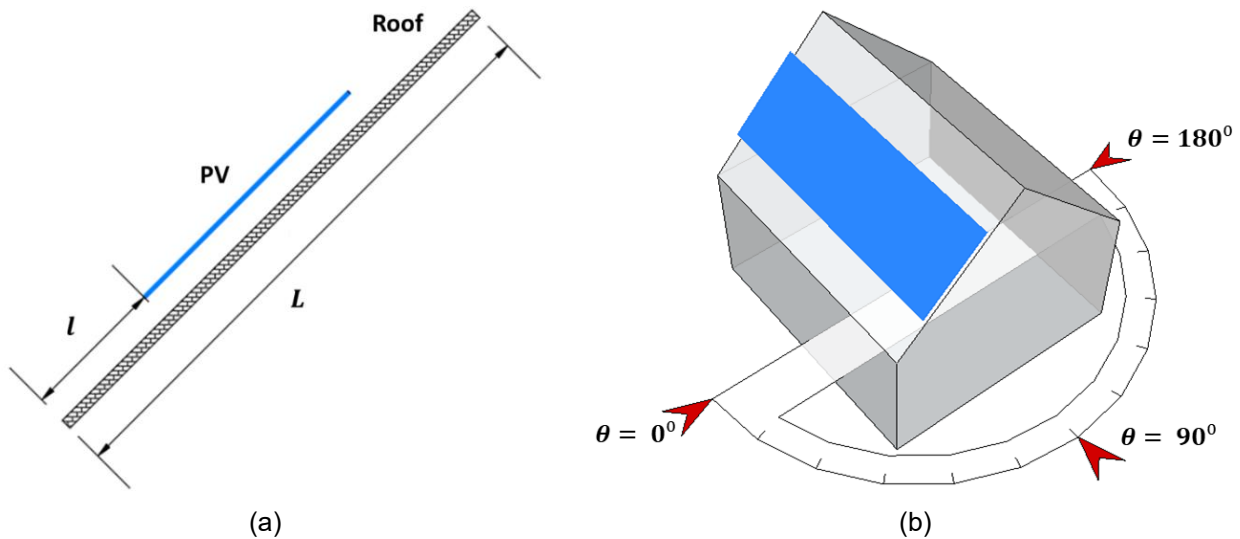
265   Figure 4 Schematic description of a) PV position index (PI) and b) relative wind angle
266   (θ) *Table* 3 demonstrates the detailed value ranges for each variable. As it can be seen, there
267   are numerous random permutation and combination of PV positions, solar radiation, wind
268   direction and wind speed. Thus, it is practical to perform a sampling procedure to find only a
269   limited number of scenarios required to be simulated with CFD that can technically represent
270   the entire range of climatic conditions and PV positions. Before selecting samples through
271   Latin Hypercube Sampling (LHS) method (Petropoulos & Srivastava 2016), a sensitivity test
272   was conducted to determine the minimum strips of each microclimate variable, so that a
273   smaller population size can be determined for the simulation. Latin Hypercube Sample
274   method is a form of stratified sampling that applied to multiple variables. In principle, the
275   method is to independently stratify each variable into N intervals with equal probability of 1/N
276   and then to pick only one random sample point in every partition for each variable (Fang, Li
277   & Sudjianto, 2005). It provides significant benefits in terms of sampling efficiency and
278   computer processing time.

(a) $PI = 0$ (b) $PI = 0.25$ (c) $PI = 0.5$
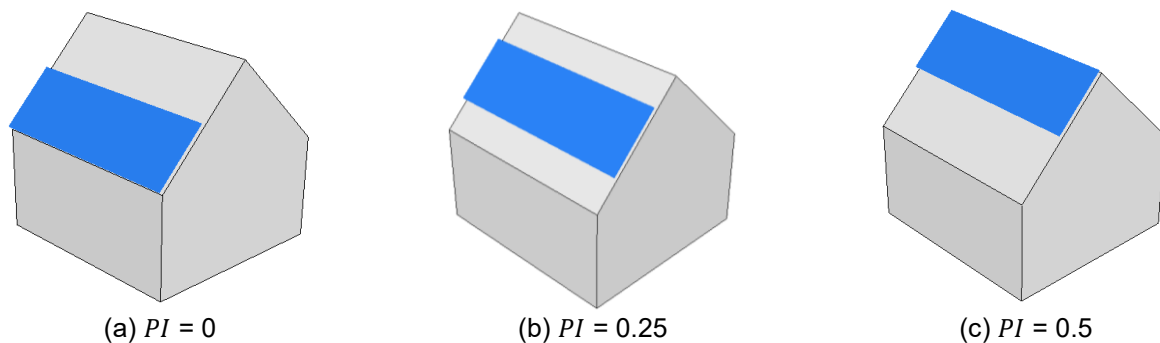
279   *Figure 5 Schematic plot of the relative positions of PV panel over the roof and their corresponding PI*

values

Table 3 Variable ranges and distributions for the sampling procedure

PV position (PI)			
Bottom	Middle	Top	Distribution
0	0.25	0.5	Uniform
Solar irradiance (G_t) & Relative wind angle (θ)			
	Left bound	Right bound	Distribution
G_t	80 W/m^2	1200 W/m^2	Uniform
θ	0°	180°	Uniform

Wind speed (U)					
Range	0.5 ~ 1 m/s	1 ~ 5 m/s	5 ~ 9 m/s	9 ~ 13 m/s	13 ~ 20 m/s
Frequency	0.0562	0.6387	0.2486	0.0456	0.0109

The benchmark case of the sensitivity analysis was defined as a PV panel mounted at the middle of the roof area ($PI = 0.25$) with a solar irradiance of 700 W/m^2 projected onto the surface while the wind was approaching opposite from the PV's orientation ($\theta = 180°$) at a speed of 3 m/s. *Table 4* lists the tested gaps of each variable for the parametric study of their impacts on the PV cell temperature (T_c) and PV surface convective heat transfer (q_c). For example, scenarios with solar irradiance of 750, 740 and 730 W/m^2 were tested to determine the sensitivity of T_c related to G_t while the critical interval was decided as one of the three studied gaps (i.e. 50, 40 and 30 W/m^2) with respect to 700 W/m^2 in benchmark case as seen in *Table 4*.

Table 4 Benchmark case and parametric controls for the sensitivity analysis

	G_t (W/m^2)	U (m/s)	θ (°)
Benchmark	700	3	180
	50	2.5	33.75
Gap to benchmark	40	2	22.5
	30	1.5	11.25

Hence, the sample size (n) can be determined by (LeBlanc, 2004):

$$n = \frac{N z_c^2 p_s (1 - p_s)}{d^2 (N - 1) + z_c^2 p_s (1 - p_s)}$$

(21)

where N is the population size, z_c is the critical value at a given confidence level, p_s is the sample proportion and d is the error margin. In this study, the confidence level and the margin error were assumed to be 95 % and 5 %, respectively; this guaranteed 95 % of the true value of population with an allowance of random error up to 5 %. The critical value for the confidence level of 95 % is 1.96 while the value of p_s is usually as 0.5 to ensure that the sample size is large enough to reflect the whole population (LeBlanc, 2004).

After deciding the sample size, Latin Hypercube Sampling method (Petropoulos & Srivastava, 2016) was used to generate evenly distributed random numbers from 0 to 1 for each investigated variable. These random numbers were then mapped into the range of each variable to fit their corresponding real values. For example, a random number of 0.773 within the range of 0-1 was indexed to 786 W/m^2 from 80-1200 W/m^2 solar irradiance range.

2.3. Multivariable fitting

After obtaining all sample results, a new regression of the cell temperature versus microclimate conditions and PV positions was developed with a nonlinear correlation using MATLAB none-linear-fit (NLINFIT) function. The benchmark formats for the solar irradiance and wind speed in the new regression were referred to their formats in accordance with the previous empirical models (i.e. NOCT and SNL). Moreover, the formats of PI and θ were proposed with a preliminary analysis of the simulation data. Curve fitting tool in MATLAB was employed to obtain a rough initial guess of coefficients for NLILFIT function and then to identify an optimum coefficient value for each term with a given explicit function format.

The results of simulations and the regression model were compared using several metrics to assess the goodness of fitting, including the coefficient of determination (R^2), the adjusted coefficient of determination ($Adjusted\ R^2$) and the root mean squared error ($RMSE$):

$$R^2 = 1 - \frac{\sum_{i=1}^{n}(Y_i - \hat{Y}_i)^2}{\sum_{i=1}^{n}(Y_i - \bar{Y}_i)^2} \tag{22}$$

$$Adjusted\ R^2 = 1 - (1 - R^2)\frac{n-1}{n - k_{coeff}} \tag{23}$$

$$RMSE = \sqrt{\frac{1}{n}\sum_{i=1}^{n}(Y_i - \hat{Y}_i)} \tag{24}$$

where Y_i and $\hat{Y}_i$ are the observed (simulated) and predicted values of each sample, respectively. $\bar{Y}$ is the mean of all Y_i and k_{coeff} is the total number of coefficients to be determined in the regression. The values of R^2 and $Adjusted\ R^2$ are within the range of 0-1 while a value closer to 1 means the regression covers more variability, thereby, is more successful in fitting to the dataset. Inversely, a smaller value of $RMSE$ is expected for a better prediction.

2.4. Qualification metrics for regression validation

Extra 40 cases (more than 10 % of sample size without being used to develop the multivariable regression model) randomly selected by Latin Hypercube Sampling were simulated to assess the validity of proposed regression. Two qualification metrics were introduced in this stage, the relative gap (E_1) and the fraction of predictions within a factor of two of observations ($FAC2$):

$$E_1 = \frac{1}{n}\sum_{i=1}^{n}\left|\frac{Y_i - \hat{Y}_i}{Y_i}\right| \tag{25}$$

$$FAC2 = \frac{1}{n}\sum_{i=1}^{n} n_i \; with \; n_i = \left\{ \begin{array}{cc} 1 & if \; 0.5 \leq \frac{\hat{Y}_i}{Y_i} \leq 2.0 \\ 0 & else \end{array} \right. \tag{26}$$

328    $FAC2$, as the one of the most robust qualification metrics, with a value closer to 1 indicates
329   a perfect matching between predictions and the observations while a $FAC2$ greater than 0.5
330   can be claimed as good enough criterion (Chang & Hanna, 2004).

3. Results

3.1. Sensitivity analysis and sampling results

333   Normalized values over the results of the benchmark case were used to illustrate the
334   sensitivity analysis. Therefore, the normalized PV cell temperature (T_c) and surface
335   convective heat flux (Q_c') for the benchmark case were defined as unity as seen in *Figure 6*.
336   It is clear that the deviation of the normalized value of tested cases over unity is increasing
337   with the interval growth of the tested variable when compared to the benchmark case. For
338   example, in *Figure 6a*, deviations of 0.04 and 0.01 of T_c and Q_c', respectively, were found for
339   the case with a same PV position, similar solar irradiance and relative wind angle to the
340   benchmark case although with having a different wind speed with a gap of 1.5 m/s. When
341   increasing the interval to 2.5 m/s, the differences of T_c and Q_c' elevated to 0.1 and 0.09,
342   respectively. A critical interval value was defined as the deviation of a case over the
343   benchmark case equal or slightly less than 0.05 in accordance with the margin error of the
344   sampling procedure. It is noteworthy that the increase of the critical interval contributes to the
345   reduction of strip amount for each variable in the specific range and thus further leads to a
346   smaller population size for the simulations. Thereby, the critical interval of wind speed was
347   determined as 1.5 m/s.

348   Similarly, the critical interval for the solar irradiance was found to be 30 W/m² considering
349   the change of Q_c' as shown in *Figure 6b*. As for the relative wind angle, seen in *Figure 6c*,
350   both normalized T_c and q_c difference for cases with interval of 11.25^0 and 22.5^0 met the
351   sensitivity requirement. To reduce the population size, 22.5^0 was then selected as the critical
352   interval for the variable θ. Therefore, the minimum required numbers of strips for the solar
353   irradiance, wind velocity and relative wind angle were calculated as 38, 13 and 9, respectively.
354   Adding three installations of the BIPV, the sampling population size was identified as 13,338
355   while the minimum sample size was found as 374 according to *Eq. 21*.

3.2. Simulation results of sample population

357   Steady state simulations of all 374 sample cases were conducted until their
358   convergences were guaranteed. The value of each variable (including wind speed, solar
359   irradiance, relative wind angle and PV position) was unique throughout all the samples as

360 selected by Latin Hypercube Sampling method. This implies that there was no two samples
361 with the same exact value for each variables. Therefore, comparisons were provided for
362 samples to investigate the impact of different variables through a parametric study that values
363 of the controlled variables were similar rather than same (only with differences less than 5 %
364 or within the range of critical interval). For example, to explore the impact of solar irradiance,
365 samples # 51 and #108 were selected with very different tested variable of G_t as 293 W/m^2
366 comparing to 1,131 W/m^2, respectively. For the rest of variables, PI is the same ($PI = 0.25$
367 for both samples) as a parametric study required; however, variable U is 3.98 m/s and
368 3.95 m/s and θ is 46° and 53° for both samples, respectively due to sample limitation. The
369 comparisons were performed through the temperature distribution plot as seen in *Figure 6-8*.
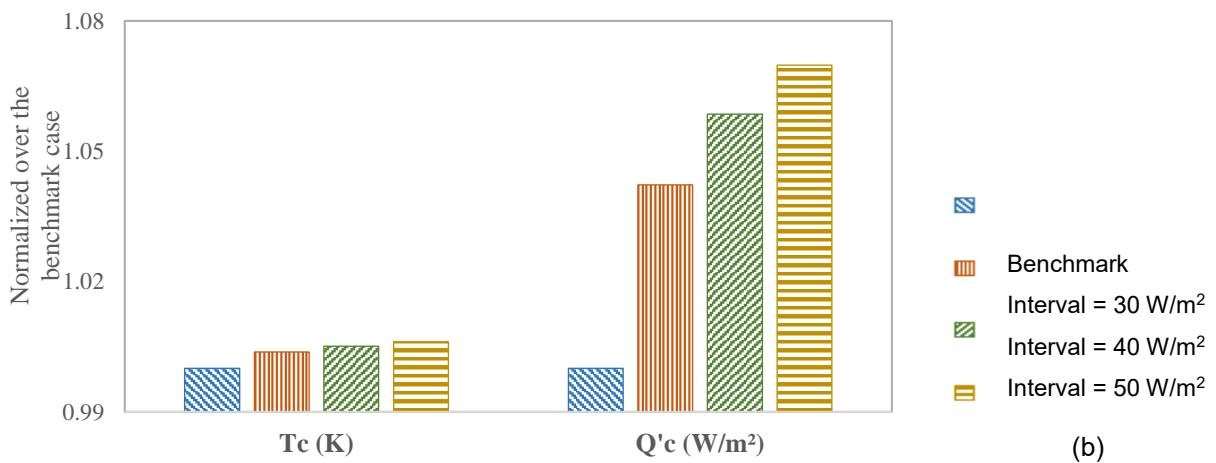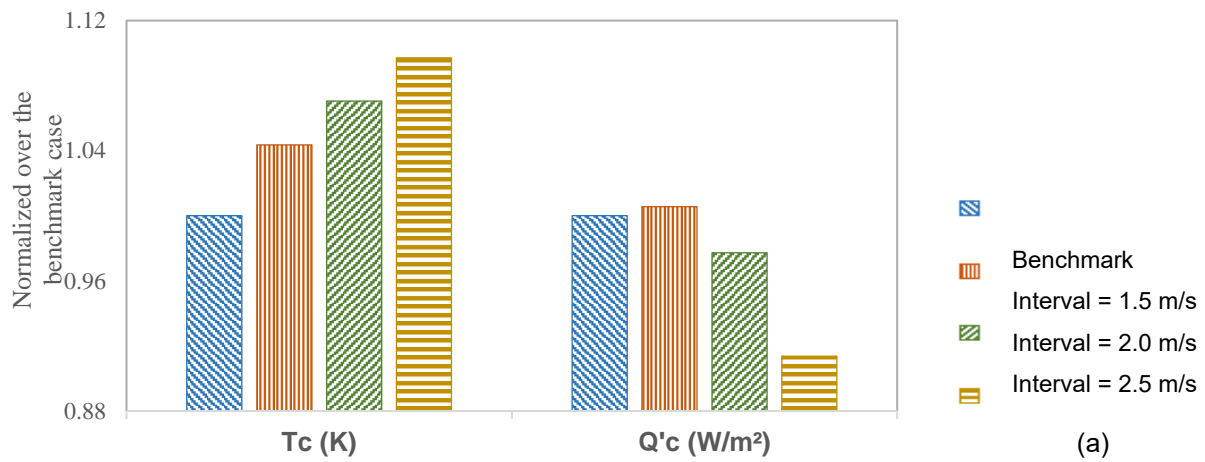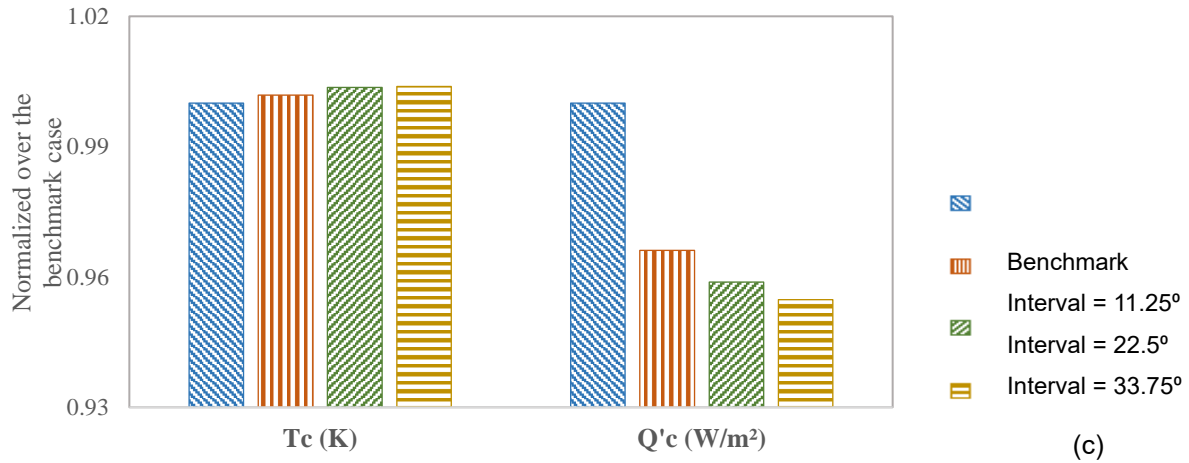
The solar irradiance (G_t) was found as the most important factor as it was similarly reflected in both existing empirical regressions (i.e. SNL and NOCT models). Based on the SNL model, the PV temperature decreases with increase of wind speed (U), however, the decreasing gradient becomes close to zero when U approaches to high values. The simulated results depicted consistent tendencies with SNL model's predictions. *Figure 7* shows a comparison of the combined effect of the solar irradiance and wind speed. In these three selected samples, the highest PV temperature occurred under the scenario with a high solar irradiance and a low wind speed. The importance of parameters G_t and U can be clearly observed by comparing *Figure 7a* versus *Figure 7b* and *Figure 7a* versus *Figure 7c*.
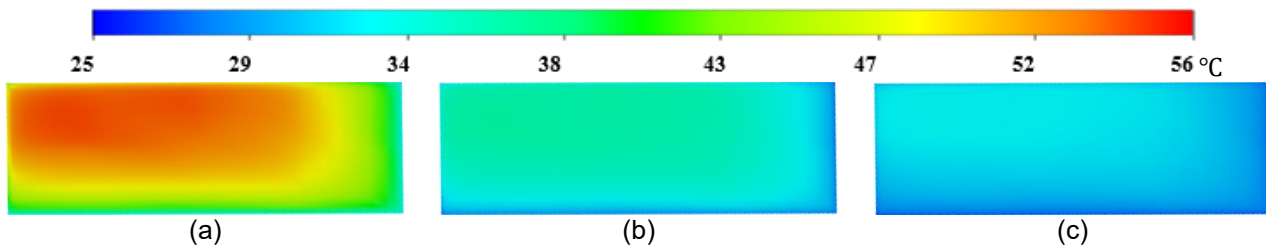
Figure 7 Temperature contour of the BIPV under scenarios of a) a high G_t with a low U; b) a high G_t with a high U and c) a low G_t with a low U
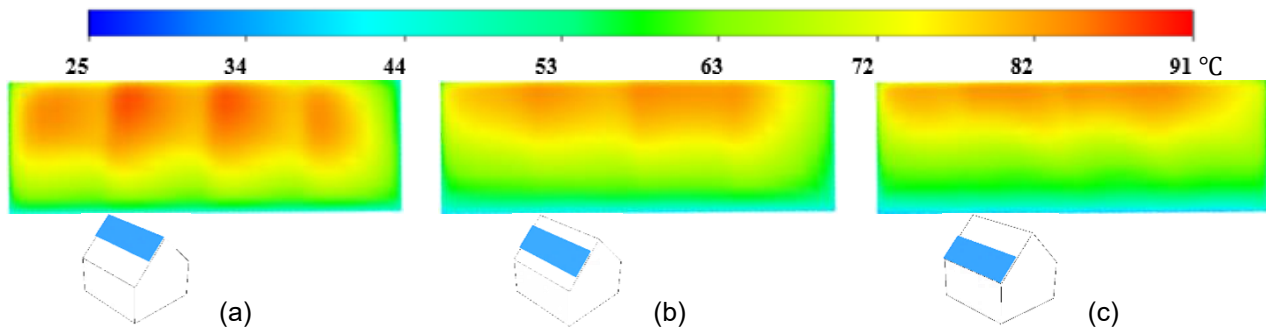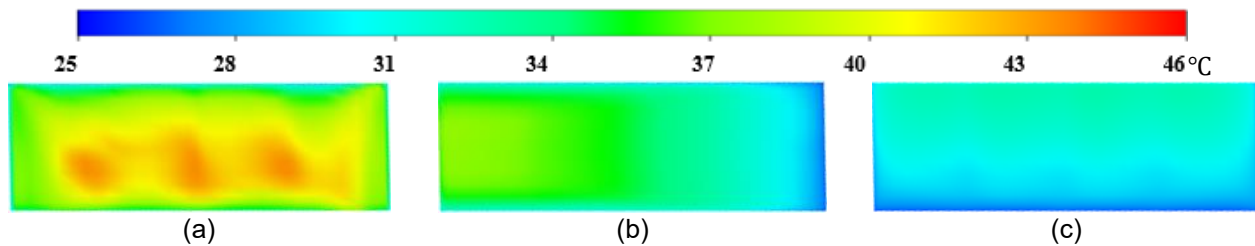

*Figure 8 Temperature contour of the BIPV placed at positions of a) $PI = 0.5$; b) $PI = 0.25$ and c) $PI = 0$*

Figure 8 compares the impact of different PV positions (PI) when the PV panels were exposed to a high solar radiation with a low speed wind approaching almost parallel to the direction of PV's orientation. As it can be seen, hot spot occurs at all three cases, however,

when the PV is placed closer to the top edge of the roof ($PI = 0.5$), the hot spot region becomes larger. It is noteworthy to specify that the solar irradiance in the scenario of *Figure 8a* (980 W/m^2) was even lower than that of for *Figure 8b* (1,122 W/m^2) and *Figure 8c* (1,151 W/m^2). This can be explained by the fact that the air becoming hotter when passing through the exposed hot roof surface and reaching to the top edge position.

Figure 9 and *Figure 10* compare the impact of the relative wind angle (θ). The investigated PV panels in both figures were placed at $PI = 0$ where a clear difference in temperature contours can be observed between *Figure 9/10a*, *Figure 9/10b* and *Figure 9/10c*. Temperature gradient is more likely to be distributed in the streamwise direction in *Figure 9*. As depicted in *Figure 10a*, air is moving downward when wind approaches from backside ($\theta = 174°$) and, therefore, a high temperature is captured at a relatively low position as seen in *Figure 9a*. In contrast, a higher temperature can be seen at the upper part of the PV surface in *Figure 9c* when air is moving upward as seen in *Figure 10c*. A higher risk of overheating is also found when wind approaches from the backside of the PV panel, which means the panels are at the leeward where surrounded by a relatively calm air. This is supported by the airflow pattern shown in the *Figure 10a*. With a similar climatic wind speed, a lower local velocity is observed for larger relative wind angles (e.g., $\theta = 174°$ compared to $\theta = 99°$ or $\theta = 4°$). Moreover, a complex hybrid impact of the relative wind angle and PV index can be seen in *Figure 9*, which is further discussed in *Section 3.3*.

(a)   (b)   (c)

Figure 9 Temperature contour of the BIPV under scenarios of a) $\theta = 174°$; b) $\theta = 99°$ and c) $\theta = 4°$

(a)   (b)   (c)
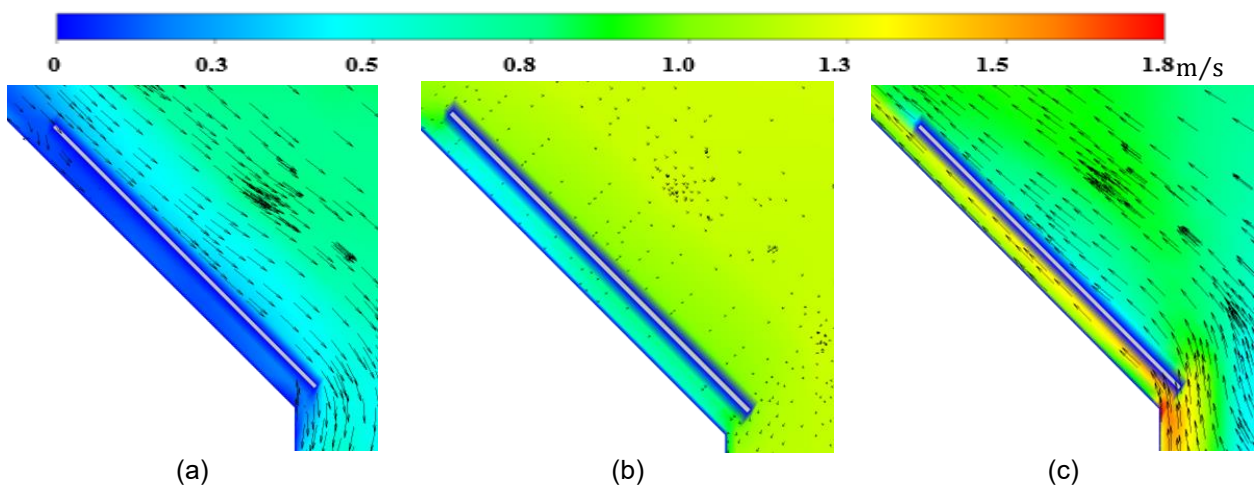
Figure 10 Velocity contour and vector plot of the airflow around BIPV under scenarios of a) $\theta = 174°$; b) $\theta = 99°$ and c) $\theta = 4°$

3.3. New regression equation from simulations

As mentioned in *Section 2.2*, the PV cell temperature was reported to be linearly related to the air temperature in all previous models. Hence, the new regression model was developed to predict temperature difference between T_c and T_a. Considering the tendency of temperature difference influenced by each variable, solar irradiance (G_t) was found as the most critical factor consistent with the expectations whilst the weighting of the PV position index (PI) was observed to be the lowest. The format of the new regression model was thus proposed as:

$$T_C - T_a = a_1 G_t^{a_2} \cdot e^{(a_3 U^{a_4} + a_5 U + a_6 \theta + a_7 PI)} + a_8 \theta \cdot PI + a_9 \tag{27}$$

where a_n are the constant coefficients and after optimization by NLINFIT function in MATLAB were found as $a_1 = 0.2743$, $a_2 = 0.8989$, $a_3 = -0.9832$, $a_4 = 0.5777$, $a_5 = 0.181$, $a_6 = 0.0018$, $a_7 = -0.0118$, $a_8 = -0.0424$, $a_9 = -0.9566$.
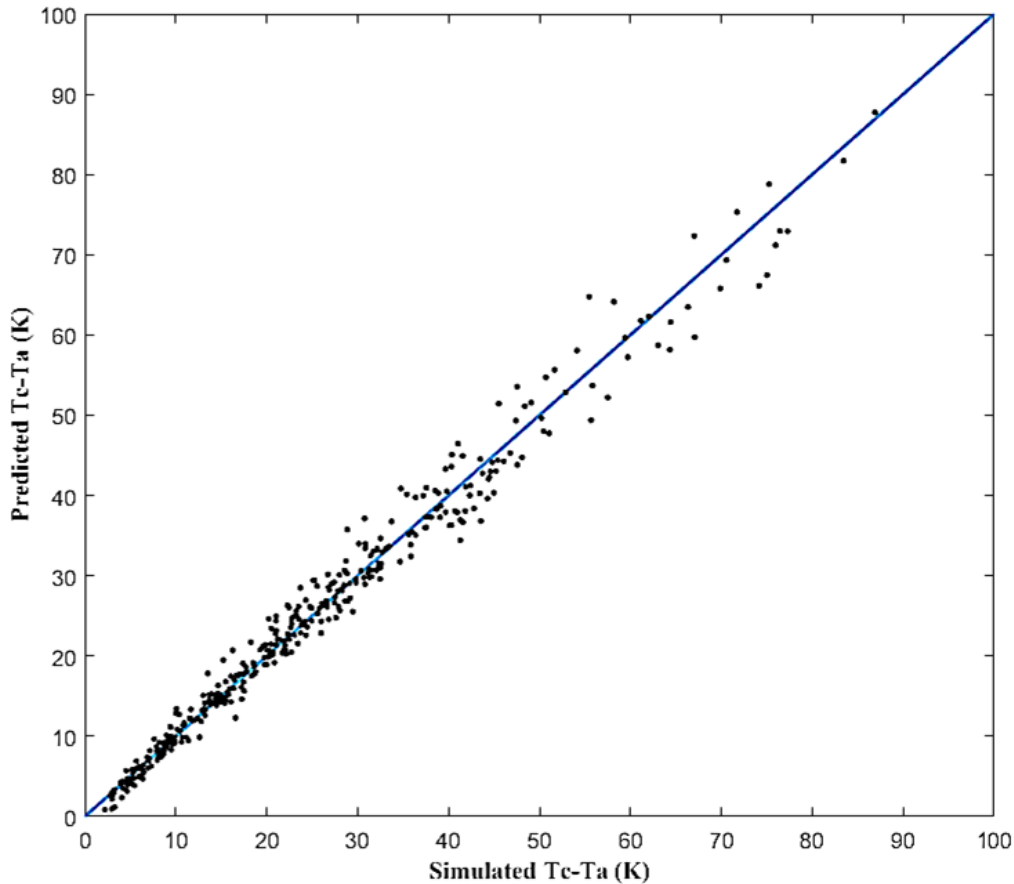
Figure 11 Prediction of $T_c - T_a$ by the proposed regression model (black dots) and simulation results (blue line)

The validity of the proposed regression model has been evaluated as displayed in *Figure 11*. The predicted results distribute evenly around the blue straight line (with a gradient of unity), indicating the simulated values. The goodness of fitting evaluated from *Eq. 22-24* was reported as R^2 =0.9813, $Adjusted\ R^2$ =0.9809 and $RMSE$ = 2.3674. Therefore, a high fitting quality was concluded from a high $Adjust\ R^2$ of 0.9809. As RMSE has the same unit as the

430 dependent variable, the value of 2.3674 K can be regarded as a small value in accordance
431 with the range of $T_c - T_a$ defined between 0 K and 100 K.

(a)

(b)
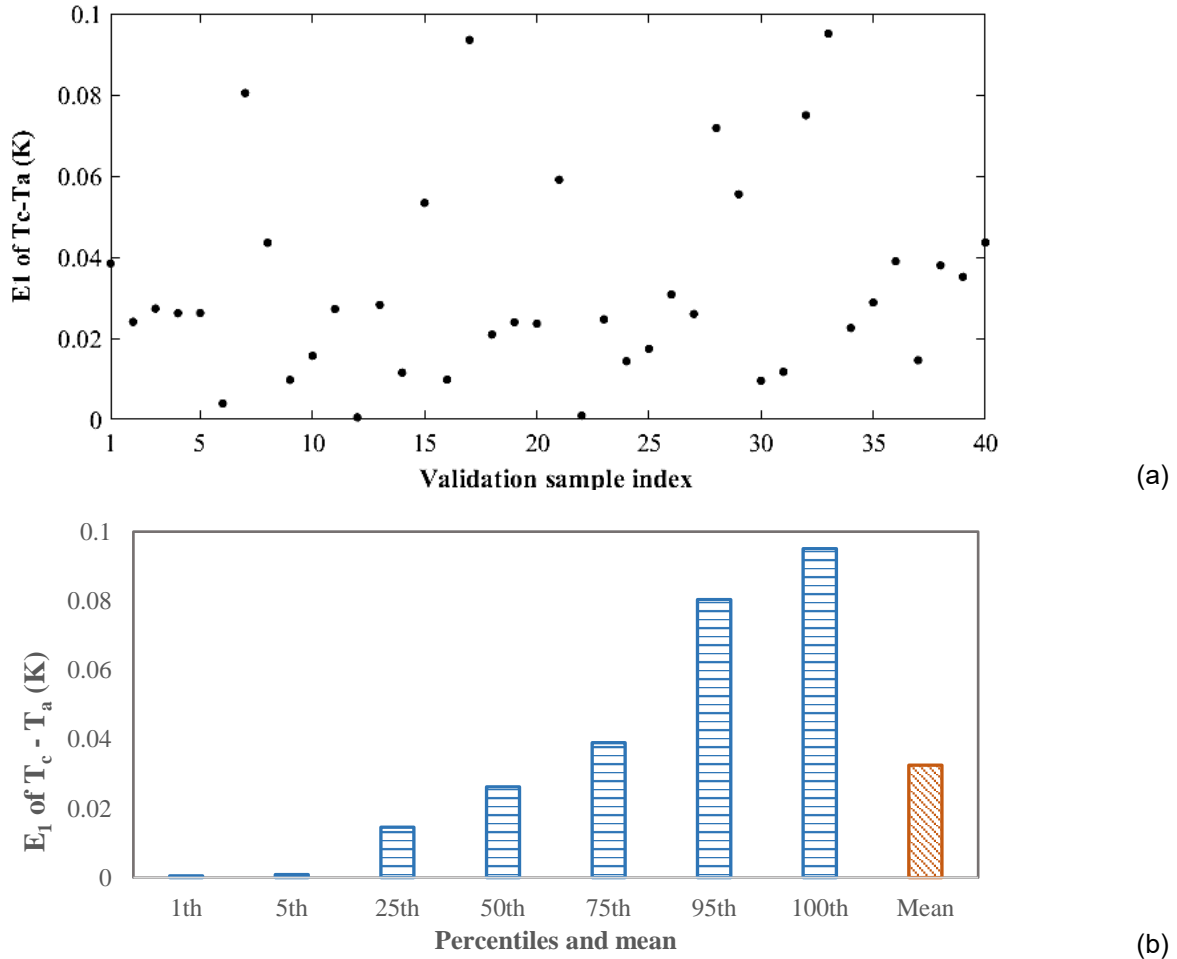
432 *Figure 12 E_1 of $T_c - T_a$ between predictions by proposed regression model and simulations for a) each*
433 *sample case and b) different percentile and the mean value*

3.4. Validation of new regression

435   *Figure 12* plots the relative gap of $T_c - T_a$ between the prediction by proposed new
436 regression model and the CFD simulation of 40 extra sample scenarios for the validation
437 purpose, which were not initially included in the fitting procedure. Approximately 80% of 40
438 cases were found to have a small gap (less than 0.05) between predictions and simulations
439 while the 75th percentile of E_1 (see *Eq. 25*) was around 0.039. The mean value of E_1 was
440 found as 0.0325, slightly higher than the median value of 0.0262. Larger E_1 occurred under
441 the condition where a low speed wind was approaching from backside of the BIPV with a
442 large θ while the panel was placed closer to the top edge. For example, under a scenario of
443 $PI = 0.5$, $G_t = 201 \text{ W/m}^2$, $\theta = 174°$ and $U = 0.55 \text{ m/s}$, the predicted temperature difference
444 between the PV cell and ambient was 23.10K comparing to the simulated value of 19.49 K;
445 E_1 was thereby calculated as 0.0749, which was relatively high among 40 sample cases. The
446 possibility of occurrence of extreme conductions (e.g. E_1 exceeds 0.9) was within 5 %.
447 Moreover, the $FAC2$ value (see *Eq. 26*) of 40 validation cases was equal to 1. Therefore, it
448 can be concluded that the proposed regression model is highly valid to predict the simulated

449   cell temperature of PV panels.

450   *Figure 13* presents the predicted $T_c - T_a$ by the new regression and SNL model. For
451   individual cases that the SNL model delivers a higher temperature difference with, the
452   prediction given by the new regression model would also be relatively higher. In general, an
453   obvious underestimation of T_c by the SNL model can be observed when comparing to the
454   prediction by the new regression model. The R^2 of results by two models is approximately
455   0.4760, indicating rather big deviations. A potential reason of this phenomena is due to the
456   fact that the assumption of open-rack installed PV panels with sufficient cooling in the SNL
457   model is not always realistic. Also, as the new proposed regression model was obtained from
458   computational simulations, the relative discrepancies from the experimental measurements
459   should be taken into account.
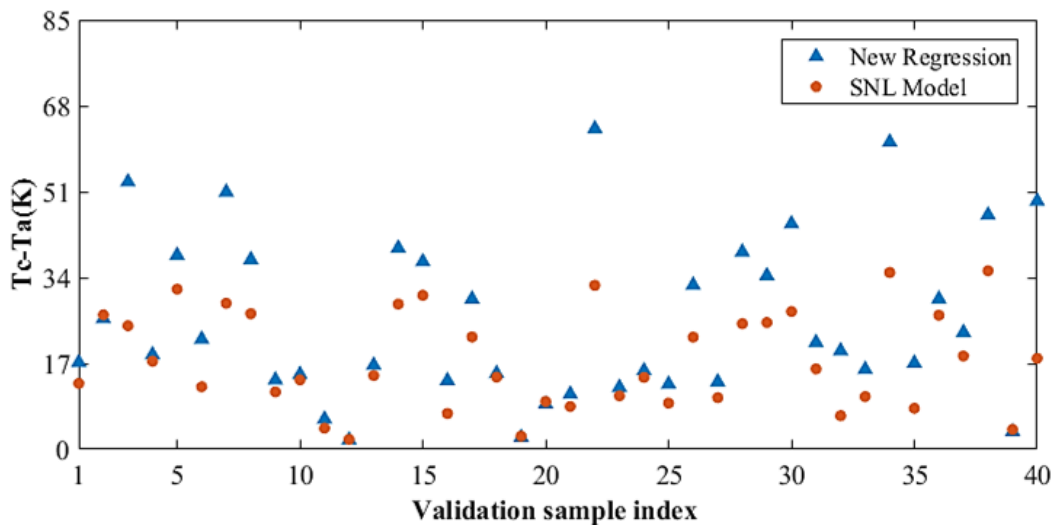
460
461   *Figure 13 Predicted $T_c - T_a$ by the new proposed regression and SNL models*

4. Conclusion

463   In summary, a new regression model for prediction of the BIPV cell temperature was
464   proposed from a series of full-scaled BIPV CFD simulations. The ambient temperature, solar
465   irradiance, wind speed, relative wind angle and PV position (PV position index) over the roof
466   were taken into account as the influential parameters on the PV cell temperature. Using the
467   sensitivity analysis and Latin Hypercube Sampling approach, the minimum size of the
468   population and sampling size were identified as 13,338 and 374, respectively. Thus,
469   simulations of sample cases were conducted to qualify and quantify the relationship between
470   climatic variables, PV position and PV cell temperature. The simulation results demonstrated
471   the following primary relationships among each variable and $T_c - T_a$:

472   ➢ It was found that the solar irradiance and wind speed were of the most important factors
473   in determining the BIPV cell temperature while the PV position was the least.

474   ➢ Higher temperature differences were presented under high solar irradiances.

475   ➢ The PV panel can be cooled down against strong wind conditions. However, there existed
476   a critical value in which, if the wind speed exceeded, the growth of cooling effect would

21

477   become weak.

478 ➢ The impacts of relative wind angle and wind direction were found to be complex while the
479   possibility of a hybrid influence of two variables was observed.

480 ➢ Based on the simulation results and observed phenomena, the regression model was
481   proposed with satisfying substantial indicators of goodness-of-fit. 80 % of validation cases
482   were found successfully predicting $T_c - T_a$ with a relative error of less than 5 %.

483 The main aim of this study was to provide a systematic way to predict the BIPV performance
484 rather than using the existing empirical correlations. Thus, the future work will be focused on
485 development of experimental measurement set ups to measure the certainty of the regression
486 model proposed in this study.

Acknowledgment

References

491 Assoa, Y. B., Gaillard, L., Ménézo, C., Negri, N., & Sauzedde, F. (2018). 'Dynamic prediction of a
492   building integrated photovoltaic system thermal behaviour', *Applied Energy*, 214: 73-82.
493 Bagatelos, N., & Henson, J. W. C. (2012). "BIPV Facades Reconsidered: Mid-rise and High Rise
494   Applications." In *the Third Building Enclosure Science & Technology Conference (BEST)*. Atlanta,
495   Geogia, USA.
496 Bahaj, A. S. (2003). 'Photovoltaic roofing: issues of design and integration into buildings', *Renewable*
497   *Energy*, 28: 2195-204.
498 Bramanti, O. (2015). *Solar Power Conversion - Engineering, Technology, Financing* (Youcanprint).
499 Chang, J. C., & Hanna, S. R. (2004). 'Air quality model performance evaluation', *Meteorology and*
500   *Atmospheric Physics*, 87: 167-96.
501 Chen, B., Clark, D., Maloney, J., Mei, W. & Kasher. J. (1995). "Measurement of night sky emissivity in
502   determining radiant cooling from cool storage roofs and roof ponds." In *Proceedings of the*
503   *National Passive Solar Conference*, 310-13. AMERICAN SOLAR ENERGY SOCIETY INC.
504 D'Orazio, M., Perna, C. D. & Giuseppe, E. D. (2014). 'Experimental operating cell temperature
505   assessment of BIPV with different installation configurations on roofs under Mediterranean
506   climate', *Renewable Energy*, 68: 378-96.
507 Department of Energy U.S. (2016). "EnergyPlus Engineering Reference." In.
508 Elkarmi, F., & Abu-Shikhah, N. (2012). *Power System Planning Technologies and Applications:*
509   *Concepts, Solutions and Management* (IGI Global: Hershey, PA, USA).
510 ElSayed, M. S. (2016). 'Optimizing thermal performance of building-integrated photovoltaics for
511   upgrading informal urbanization', *Energy and Buildings*, 116: 232-48.
512 Energy Information Administration. (2017). "International Energy Outlook 2017." In.
513 Fang, K.T., Li, R. & Sudjianto, A. (2005). *Design and Modeling for Computer Experiments* (CRC Press).
514 Gan, G. (2009a). 'Effect of Air Gap on the Performance of Building-integrated Photovoltaics', *Energy*,
515   34: 913-21.
516 Gan, G. (2009b). 'Numerical Determination of Adequate Air Gaps for Building-integrated
517   Photovoltaics', *Solar Energy*, 83: 1253-73.

518 Gliah, O., Kruczek, B., Gh. Etemad, S. & Thibault, J. (2011). 'The effective sky temperature: an
519   enigmatic concept', *Heat and Mass Transfer*, 47: 1171-80.
520 Gökmen, N., Hu, W., Hou, P., Chen, Z., Sera, D. & Spataru, S. (2016). 'Investigation of wind speed
521   cooling effect on PV panels in windy locations', *Renewable Energy*, 90: 283-90.
522 Goldemberg. (2000). "World Energy Assessment: Energy and the Challenge of Sustainability." In.
523 Hemmer, C., Saad, A. A., Popa, C. V. & Polidori, G. (2017). 'Early development of unsteady convective
524   laminar flow in an inclined channel using CFD: Application to PV panels', *Solar Energy*, 146:
525   221-29.
526 Jubayer, C. M. (2014). 'Wind and Thermal Effects on Ground Mounted Photovoltaic (PV) Panels', The
527   University of Western Ontario.
528 Jubayer, C. M., Karava, P., & Savory, E. (2010). "CFD Simulations for Evaluation of Forced Convective
529   Heat Transfer Coefiicents on Photovoltaic/Thermal Systems Integrated on the Windward
530   Roof Surface of a Low-rise Building." In *The Fifth nternational Symposium on Computational
531   Wind Engineering (CWE2010)*. Chapel Hill, North Carolina, USA.
532 Kaldellis, J. K., Kapsali, M. & Kavadias, K. A. (2014). 'Temperature and wind speed impact on the
533   efficiency of PV installations. Experience obtained from outdoor measurements in Greece',
534   *Renewable Energy*, 66: 612-24.
535 Kalogirou, S. A. (2014). *Solar Energy Engineering* (Elsevier Inc.: Oxford).
536 Karava, P., Jubayer, C. M., Savory, E., & Li, S. (2012). 'Effect of Incident Flow Conditions on Convective
537   Heat Transfer from the Inclined Windward Roof of a Low-rise Building with Application to
538   Photovoltaic-thermal Systems', *Journal of Wind Engineering and Industrial Aerodynamics*,
539   104–106: 428-38.
540 King, D. L., Boyson, W. E., & Kratochvill, J. A. (2004). "Photovoltaic Array Performance Model." In.
541   Albuquerque: Sandia National Laboratories.
542 Koyunbaba, B. K., Yilmaz, Z., & Ulgen, K. (2013). 'An Approach for Energy Modeling of a Building
543   Integrated Photovoltaic (BIPV) Trombe Wall System', *Energy and Buildings*, 67: 680-88.
544 LeBlanc, D.C. (2004). *Statistics: Concepts and Applications for Science* (Jones and Bartlett).
545 Liao, L., Athienitis, A. K., Candanedo, L., Park, KW., Poissant, Y., & Collins, M. R. (2005). "Numerical
546   Study of Conjugate Heat Transfer in a BIPV-Thermal System." In *ASME 2005 International
547   Solar Energy Conference*. Orlando, Florida, USA.
548 Markvart, T., & Bogus, K. (2000). *Solar Electricity* (Wiley).
549 Mirzaei, P. A., & Carmeliet, J. (2013). 'Dynamical computational fluid dynamics modeling of the
550   stochastic wind for application of urban studies', *Building and Environment*, 70: 161-70.
551 Mirzaei, P. A., & Carmeliet, J. (2015). 'Influence of the underneath cavity on buoyant-forced cooling
552   of the integrated photovoltaic panels in building roof: a thermography study', *Progress in
553   Photovoltaics: Research and Applications*, 23: 19-29.
554 Mirzaei, P. A., and Haghighat, F. (2012). 'A procedure to quantify the impact of mitigation techniques
555   on the urban ventilation', *Building and Environment*, 47: 410-20.
556 Mirzaei, P. A., Paterna, E., & Carmeliet, J. (2014). 'Investigation of the role of cavity airflow on the
557   performance of building-integrated photovoltaic panels', *Solar Energy*, 107: 510-22.
558 Mirzaei, P. A., & Zhang, R. (2015). 'Validation of a Climatic CFD Model to Predict the Surface
559   Temperature of Building Integrated Photovoltaics', *Energy Procedia*, 78: 1865-70.
560 Nordmann, T., & Clavadetscher, L. (2003). "Understanding Temperature Effects on PV System
561   Performance." In *Proceedings of the Third World Conference on Photovoltaic Energy
562   Conservion*. Osaka, Japan.
563 Panwar, N. L., Kaushik, S. C., & Kothari, S. (2011). 'Role of renewable energy sources in environmental
564   protection: A review', *Renewable and Sustainable Energy Reviews*, 15: 1513-24.

Petropoulos, G., & Srivastava, P.K. (2016). *Sensitivity Analysis in Earth Observation Modelling* (Elsevier Science).

Reagan, J. A., & Acklam, D. M. (1979). 'Solar reflectivity of common building materials and its influence on the roof heat gain of typical southwestern U.S.A. residences', *Energy and Buildings*, 2: 237-48.

Renewable Energy Policy Network for the 21st Century. (2017). "Reneawables 2017 Global Status Report." In.

Ross Jr, RG. (1976). "Interface design considerations for terrestrial solar cell modules." In *12th Photovoltaic Specialists Conference*, 801-06.

Skoplaki, E., & Palyvos, J. A. (2009). 'Operating temperature of photovoltaic modules: A survey of pertinent correlations', *Renewable Energy*, 34: 23-29.

Solanki, C. S. (2013). *Solar Photovoltaic Technology and Systems* (Prentice-Hall of India Pvt. Ltd.: Delhi).

Teo, H. G., Lee, P. S., & Hawlader, M. N. A. (2012). 'An active cooling system for photovoltaic modules', *Applied Energy*, 90: 309-15.

Tominaga, Y., Mochida, A., Yoshie, R., Kataoka, H., Nozu, T., Yoshikawa, M., & Shirasawa, T. (2008). 'AIJ guidelines for practical applications of CFD to pedestrian wind environment around buildings', *Journal of Wind Engineering and Industrial Aerodynamics*, 96: 1749-61.

Vautard, R., Cattiaux, J., Yiou, P., Thépaut, JN., & Ciais, P. (2010). 'Northern Hemisphere atmospheric stilling partly attributed to an increase in surface roughness', *Nature Geoscience*, 3: 756.

Wilson, M. J., & Paul, M. C. (2011). 'Effect of Mounting Geometry on Convection Occurring Under a Photovoltaic Panel and the Corresponding Efficiency Using CFD', *Solar Energy*, 85: 2540-50.

Zhang, R., Mirzaei, P. A., & Carmeliet, J. (2017). 'Prediction of the surface temperature of building-integrated photovoltaics: Development of a high accuracy correlation using computational fluid dynamics', *Solar Energy*, 147: 151-63.

Zogou, O., & Stapountzis, H. (2012). 'Flow and heat transfer inside a PV/T collector for building application', *Applied Energy*, 91: 103-15.